Available online at www.sciencedirect.com
SCIENCE DIRECT®
ELSEVIER
European Journal of Mechanics B/Fluids 23 (2004) 339–351
EUROPEAN JOURNAL OF MECHANICS B/FLUIDS

Numerical simulation of 3-D incompressible, multi-phase flows over cavitating projectiles

Farouk M. Owis, Ali H. Nayfeh *

Department of Engineering Science and Mechanics, MC 0219, Virginia Polytechnic Institute and State University Blacksburg, VA 24061, USA

Received 18 February 2003; received in revised form 19 August 2003; accepted 13 October 2003

Abstract

The hydrodynamic cavitation over axisymmetric projectiles is computed using the unsteady incompressible Navier–Stokes equations for multi-fluid elements. The governing equations are discretized on a structured grid using an upwind difference scheme with flux limits. A preconditioning dual-time stepping method is used for the unsteady computations. The eigensystem is derived for the Jacobian matrices. This eigensystem is suitable for high-density ratio multi-fluid flows and it provides high numerical stability and fast convergence. This method can be used to compute single- as well as multi-phase flows. Cavitating flows over projectiles with different geometries are computed and the results are in good agreement with available experimental data and other published computations.

Keywords: Unsteady; Incompressible; Cavitation; Upwind; Preconditioning

1. Introduction

The current work is motivated by recent efforts to develop high-speed under water vehicles. Cavitation plays an important role in the development of such vehicles because of the unsteady features associated with this type of flow. It causes unsteady hydrodynamic forces, severe noise, structural erosion, and vibration problems. In order to control these problems, it is necessary to predict accurately the extent and behavior of the cavitating flow on the body surface. On the other hand, cavitation reduces the viscous drag significantly on the body surface. Thus, it is possible to reach high speeds under the water because of cavitation. It might occur partially on the body surface or it might grow until it becomes very long compared with the body dimensions; the latter is called supercavitation. Cavitation occurs as a result of the flow acceleration over the body surface resulting in regions with pressures lower than the evaporation pressure. Then the water evaporates in these regions, thereby forming vapor-filled cavities. These cavities tend to collapse due to the reentrant of a water jet and the flow becomes unsteady. Thus an irregular cyclic process of bubble formation and growth occurs, followed by the filling and finally breaking off of the bubble.

Due to cavitation, large density and viscosity gradients arise at the interfaces between nearly incompressible fluids. Accurate prediction of this fluid flow, where sharp interfaces might occur, represents a numerical problem of considerable difficulty. Many strategies are adopted to deal with this flow, including volume-tracking [1,2] and front-tracking [3–5] methods.

Another technique, which is used by many authors [6–13] is the Eulerian approach where separate equations are used to describe each phase. Two different formulations of the governing equations are usually used to capture the interface, namely the multi-fluid model and the mixture model. The multi-fluid model is formulated by considering a set of conservation equations for each phase and interaction terms at the interfaces are added to the equations as source terms [14]. For the mixture model, the momentum equations are described for the mixture while a separate continuity equation is employed for each phase. One

* Corresponding author.
E-mail address: anayfeh@vt.edu (A.H. Nayfeh).

0997-7546/$ – see front matter
doi:10.1016/j.euromechflu.2003.10.005

of the phasic continuity equations may be replaced by the mixture continuity equation in other formulations of the mixture model [11,12]. In the current work, separate volume fraction equations are employed to represent the phase change in addition to the mixture continuity and momentum equations.

In order to predict the cavitation, a physical understanding of the cavitation process is required to model the mass-transfer rates from water to vapor or from vapor to water where the cavity might be exposed to a pressure higher than the critical pressure. A model is used by Merkle et al. [10] for the evaporation and condensation processes. In this model, the mass-transfer rate from water to vapor is set proportional to the volume fraction of the two fluids and the difference between the local and evaporation pressures.

The objective of the present work is to build an algorithm for the prediction of super- and partial cavitation over submerged bodies. We focus on the numerical problems associated with this type of flow, especially at the interface where high-order accurate numerical methods can cause some numerical oscillations. A dual-time stepping method is used for the unsteady computations by introducing artificial time terms in the governing equations.

Turbulence modeling is employed for this multi-phase system to model the fine Kolmogorov scales where equilibrium of the turbulence scales at the interface is assumed. In the current computations, interactions between the transported dispersed-phase and field turbulence are treated on the basis of one-way coupling where the momentum exchange between the multi-phase system is assumed to have negligible effect on the turbulence generation in the liquid phase. Therefore, no source terms are added to the turbulence equations to account for the phase change at the interface. In addition, the transported phase in this bubbly flow is assumed to be larger than the Kolmogorov scales. Thus, closure relationships for turbulence are used to approximate the mechanical turbulent stresses arising from the Reynolds averaging of the governing equations. In the current study, a modified two-equation k–ω model is used to model the fine-scale turbulence. This turbulence model is based on the k–ω model developed by Menter [15], which performs very well in case of adverse pressure-gradient flows. A different formulation of the model is used by Rogers [16] to remove the freestream dependency of this model by implementing a zonal approach, which automatically switches from the Wilcox model [17] in the near wall region to an equivalent k–ε model [18] away from the wall. The model is modified in the current work to account for the density variations across the interface between the different flow phases.

2. Governing equations

The mixture model is used in the current work for the numerical simulation of cavitating flows. In this model, the flow is assumed to be in thermal and dynamic equilibrium at the interface where the flow velocity is assumed to be continuous. Thus, the momentum equations are used to describe the fluid mixture while a single continuity equation is used for each fluid component. The phasic continuity equations are written in terms of the volume fraction (α_i).

The equations are described for a fluid mixture of liquid, vapor, and non-condensable gas. The vapor continuity equation is replaced by the mixture continuity equation to simplify the derivation of the eigensystem. Source terms are added to the mixture and liquid continuity equations to model the mass-transfer rates from liquid to vapor ($\dot{m}_l$) and from vapor to liquid ($\dot{m}_v$). Hence, the governing equations can be written in the following Cartesian form:

$$\frac{1}{\beta}\frac{\partial p}{\partial \tau} + \frac{\partial u_j}{\partial x_j} = \left(\frac{1}{\rho_l} - \frac{1}{\rho_v}\right)(\dot{m}_v + \dot{m}_l), \tag{1}$$

$$\frac{\partial \rho_m u_i}{\partial t} + \frac{\partial \rho_m u_i}{\partial \tau} + \frac{\partial \rho_m u_i u_j}{\partial x_j} = \frac{\partial p}{\partial x_i} + \frac{\partial}{\partial x_j}\left[(\mu_m + \mu_t)\left(\frac{\partial u_i}{\partial x_j} + \frac{\partial u_j}{\partial x_i}\right)\right] + \rho_m g_i, \tag{2}$$

$$\frac{\partial \alpha_l}{\partial t} + \frac{\partial \alpha_l}{\partial \tau} + \frac{\alpha_l}{\beta}\frac{\partial p}{\partial \tau} + \frac{\partial \alpha_l u_j}{\partial x_j} = \frac{1}{\rho_l}(\dot{m}_v + \dot{m}_l), \tag{3}$$

$$\frac{\partial \alpha_g}{\partial t} + \frac{\partial \alpha_g}{\partial \tau} + \frac{\alpha_g}{\beta}\frac{\partial p}{\partial \tau} + \frac{\partial \alpha_g u_j}{\partial x_j} = 0, \tag{4}$$

where β is the artificial compressibility parameter, τ is the artificial time, and t is the physical time.

The mixture density can be calculated from the volume fraction as follows:

$$\rho_m = \alpha_l \Delta\rho_l + \alpha_g \Delta\rho_g + \rho_v, \tag{5}$$

$$\Delta\rho_i = \rho_i - \rho_v, \tag{6}$$

where the subscripts l, v and g denote liquid phase, vapor phase and non-condensable gas, respectively.

Artificial time terms are added to the governing equations in order to build up a dual-time stepping algorithm for the unsteady calculations. The suggested artificial terms ensure a consistent convergence rate in the different flow regions.

The governing equations are normalized with the liquid density ρ_l, freestream axial velocity, and the characteristic length of the body. The equations can be rewritten in generalized curvilinear coordinates as follows:

$$\Gamma_e \frac{\partial \widehat{Q}}{\partial t} + \Gamma \frac{\partial \widehat{Q}}{\partial \tau} + \frac{\partial (F - F_v)}{\partial \xi} + \frac{\partial (G - G_v)}{\partial \eta} + \frac{\partial (H - H_v)}{\partial \zeta} - \widehat{S} = 0, \tag{7}$$

$$\widehat{Q} = \frac{Q}{J} = \frac{1}{J}(p, u_1, u_2, u_3, \alpha_l, \alpha_g)^{\mathrm{T}}, \tag{8}$$

$$F = \frac{1}{J}(U_1, \rho_m u_1 U_1 + \xi_{x1} p, \rho_m u_2 U_1 + \xi_{x2} p, \rho_m u_2 U_1 + \xi_{x2} p, \alpha_l U_1, \alpha_g U_1)^{\mathrm{T}}, \tag{9}$$

$$G = \frac{1}{J}(U_2, \rho_m u_1 U_2 + \eta_{x1} p, \rho_m u_2 U_2 + \eta_{x2} p, \rho_m u_3 U_2 + \eta_{x3} p, \alpha_l U_2, \alpha_g U_2)^{\mathrm{T}}, \tag{10}$$

$$H = \frac{1}{J}(U_3, \rho_m u_1 U_3 + \zeta_{x1} p, \rho_m u_2 U_3 + \zeta_{x2} p, \rho_m u_3 U_3 + \zeta_{x3} p, \alpha_l U_3, \alpha_g U_3)^{\mathrm{T}}, \tag{11}$$

$$U_1 = \xi_{x1} u_1 + \xi_{x2} u_2 + \xi_{x3} u_3, \tag{12}$$

$$U_2 = \eta_{x1} u_1 + \eta_{x2} u_2 + \eta_{x3} u_3, \tag{13}$$

$$U_3 = \zeta_{x1} u_1 + \zeta_{x2} u_2 + \zeta_{x3} u_3, \tag{14}$$

$$\begin{aligned} F_v = \frac{\mu_m + \mu_t}{J\,Re}\Bigg(0, &(\nabla\xi\cdot\nabla\xi)\frac{\partial u_1}{\partial \xi} + (\nabla\xi\cdot\nabla\eta)\frac{\partial u_1}{\partial \eta} + (\nabla\xi\cdot\nabla\zeta)\frac{\partial u_1}{\partial \zeta},\\ &(\nabla\xi\cdot\nabla\xi)\frac{\partial u_2}{\partial \xi} + (\nabla\xi\cdot\nabla\eta)\frac{\partial u_2}{\partial \eta} + (\nabla\xi\cdot\nabla\zeta)\frac{\partial u_2}{\partial \zeta},\\ &(\nabla\xi\cdot\nabla\xi)\frac{\partial u_3}{\partial \xi} + (\nabla\xi\cdot\nabla\eta)\frac{\partial u_3}{\partial \eta} + (\nabla\xi\cdot\nabla\zeta)\frac{\partial u_3}{\partial \zeta}, 0, 0\Bigg)^{\mathrm{T}}, \end{aligned} \tag{15}$$

$$\begin{aligned} G_v = \frac{\mu_m + \mu_t}{J\,Re}\Bigg(0, &(\nabla\eta\cdot\nabla\xi)\frac{\partial u_1}{\partial \xi} + (\nabla\eta\cdot\nabla\eta)\frac{\partial u_1}{\partial \eta} + (\nabla\eta\cdot\nabla\zeta)\frac{\partial u_1}{\partial \zeta},\\ &(\nabla\eta\cdot\nabla\xi)\frac{\partial u_2}{\partial \xi} + (\nabla\eta\cdot\nabla\eta)\frac{\partial u_2}{\partial \eta} + (\nabla\eta\cdot\nabla\zeta)\frac{\partial u_2}{\partial \zeta},\\ &(\nabla\eta\cdot\nabla\xi)\frac{\partial u_3}{\partial \xi} + (\nabla\eta\cdot\nabla\eta)\frac{\partial u_3}{\partial \eta} + (\nabla\eta\cdot\nabla\zeta)\frac{\partial u_3}{\partial \zeta}, 0, 0\Bigg)^{\mathrm{T}}, \end{aligned} \tag{16}$$

$$\begin{aligned} H_v = \frac{\mu_m + \mu_t}{J\,Re}\Bigg(0, &(\nabla\zeta\cdot\nabla\xi)\frac{\partial u_1}{\partial \xi} + (\nabla\zeta\cdot\nabla\eta)\frac{\partial u_1}{\partial \eta} + (\nabla\zeta\cdot\nabla\zeta)\frac{\partial u_1}{\partial \zeta},\\ &(\nabla\zeta\cdot\nabla\xi)\frac{\partial u_2}{\partial \xi} + (\nabla\zeta\cdot\nabla\eta)\frac{\partial u_2}{\partial \eta} + (\nabla\zeta\cdot\nabla\zeta)\frac{\partial u_2}{\partial \zeta},\\ &(\nabla\zeta\cdot\nabla\xi)\frac{\partial u_3}{\partial \xi} + (\nabla\zeta\cdot\nabla\eta)\frac{\partial u_3}{\partial \eta} + (\nabla\zeta\cdot\nabla\zeta)\frac{\partial u_3}{\partial \zeta}, 0, 0\Bigg)^{\mathrm{T}}, \end{aligned} \tag{17}$$

$$\widehat{S} = \frac{1}{J}\left\{(\dot{m}_v + \dot{m}_l)\left(1 - \frac{1}{\rho_v}\right), \rho_m g_1, \rho_m g_2, \rho_m g_3, (\dot{m}_v + \dot{m}_l)\right\}^{\mathrm{T}}. \tag{18}$$

The Reynolds number is defined as follows

$$Re = \frac{U_\infty D \rho_l}{\mu_l}. \tag{19}$$

The matrices Γ_e and Γ are given by

$$\Gamma_e = \begin{bmatrix} 0 & 0 & 0 & 0 & 0 & 0 \\ 0 & \rho_m & 0 & 0 & u_1\Delta\rho_l & u_1\Delta\rho_g \\ 0 & 0 & \rho_m & 0 & u_2\Delta\rho_l & u_2\Delta\rho_g \\ 0 & 0 & 0 & \rho_m & u_3\Delta\rho_l & u_3\Delta\rho_g \\ 0 & 0 & 0 & 0 & 1 & 0 \\ 0 & 0 & 0 & 0 & 0 & 1 \end{bmatrix}, \tag{20}$$

$$\Gamma = \begin{bmatrix} \frac{1}{\beta} & 0 & 0 & 0 & 0 & 0 \\ 0 & \rho_m & 0 & 0 & u_1\Delta\rho_l & u_1\Delta\rho_g \\ 0 & 0 & \rho_m & 0 & u_2\Delta\rho_l & u_2\Delta\rho_g \\ 0 & 0 & 0 & \rho_m & u_3\Delta\rho_l & u_3\Delta\rho_g \\ \frac{\alpha_l}{\beta} & 0 & 0 & 0 & 1 & 0 \\ \frac{\alpha_g}{\beta} & 0 & 0 & 0 & 0 & 1 \end{bmatrix}. \tag{21}$$

3. Turbulence modeling

A two-equation k–ω model is used for the turbulence closure. The model is a modified version of the model used by Rogers [16] to compute single-phase incompressible flows. This model has different coefficients, depending on the region of solution, to reduce the freestream dependency of the model. The model switches from the k–ω model near the wall to the k–ε model away from the wall. The variation of the mixture density is implemented in the current model. The model is defined as follows:

$$\frac{\partial(\rho_m k)}{\partial t} + \frac{\partial(\rho_m k u_j)}{\partial x_j} = P_k - \beta^* \rho_m \omega k + \frac{\partial}{\partial x_j}\left[(\mu_m + \sigma_k \mu_t)\frac{\partial k}{\partial x_j}\right], \tag{22}$$

$$\frac{\partial(\rho_m \omega)}{\partial t} + \frac{\partial(\rho_m \omega u_j)}{\partial x_j} = \gamma P_\omega - \beta^* \rho_m \omega^2 + \frac{\partial}{\partial x_j}\left[(\mu_m + \sigma_\omega \mu_t)\frac{\partial \omega}{\partial x_j}\right] + 2(1 - F_1)\sigma_{\omega 2}\frac{\mu_t}{k}\frac{\partial k}{\partial x_j}\frac{\partial \omega}{\partial x_j}, \tag{23}$$

$$\mu_t = \frac{\rho_m k}{\omega}, \tag{24}$$

where P_k and P_ω are the production terms, which are set proportional to the vorticity as explained by Rogers [16]. The constants in the model are blended, depending on the region of solution, to switch from the k–ω model to the k–ε model using the function F_1 as follows:

$$\phi = F_1\phi_1 + (1 - F_1)\phi_2, \tag{25}$$

where the value of F_1 is zero or one depending on the region, ϕ_1 represents constants for the k–ω Wilcox model, and ϕ_2 represents constants from the Jones and Launder [18] k–ε model.

4. Cavitation model

The mass-transfer rates $\dot{m}_l$ and $\dot{m}_v$ are required to model the cavitation. A simplified form of the Ginzburg–Landau potential is suggested by Merkle et al. [10]. In this model, the mass transfer rate $\dot{m}_l$ from liquid to vapor is proportional to the volume fraction and the amount by which the local pressure is below the vapor pressure. The mass transfer rates are given by the following expressions

$$\dot{m}_l = \left(\frac{c_{\text{evap}}}{t_\infty}\right)\alpha_l \,\text{Min}[0,\, p - p_v], \tag{26}$$

$$\dot{m}_v = \left(\frac{c_{\text{prod}}}{t_\infty}\right)(1 - \alpha_l - \alpha_g)\,\text{Max}[0,\, p - p_v]. \tag{27}$$

Here, t_∞ is the characteristic time of the problem and p_v is the vapor pressure, which is defined in terms of the cavitation number σ as follows:

$$\sigma = 2(p_v - p_\infty), \tag{28}$$

where the freestream pressure $p_\infty$and the vapor pressure p_v are in non-dimensional form and they are normalized with respect to the dynamic pressure ($\rho_l U_\infty^2$). The constants (c_{evap}/t_∞) and (c_{prod}/t_∞) are empirical constants, which express the time rate of the evaporation and condensation processes with respect to the flow process. In general, the source terms added to the governing equations are proportional to the vapor–liquid density ratio (ρ_v/ρ_l). Therefore, the evaporation and the production constants depend on the assumed value of the vapor–liquid density ratio. The following values are used in all of the simulations: $c_{\text{evap}}/t_\infty = 0.9$ and $c_{\text{prod}}/t_\infty = 0.9$ for $\rho_v/\rho_l = 0.0001$.

5. Numerical discretization

5.1. System eigenvalues and eigenvectors

Upwind difference schemes, such as the Roe Scheme [19], are based on the characteristics of the governing equations. Therefore, the eigenvalues and eigenvectors of the incompressible multi-phase system are required for the numerical discretization of the convective flux. The convective flux in Eq. (7) can be linearized as follows:

$$\Gamma\frac{\partial\widehat{Q}}{\partial\tau}+\Gamma_e\frac{\partial\widehat{Q}}{\partial t}+\Gamma\tilde{\mathrm{A}}\frac{\partial\widehat{Q}}{\partial\xi}+\Gamma\widetilde{\mathrm{B}}\frac{\partial\widehat{Q}}{\partial\eta}+\Gamma\widetilde{\mathrm{C}}\frac{\partial\widehat{Q}}{\partial\zeta}=\overline{S}, \tag{29}$$

$$\tilde{A}=\Gamma^{-1}\hat{A}, \tag{30}$$

where the matrix $\hat{A}$ is given by

$$\hat{A}=\frac{\partial F}{\partial\widehat{Q}}=\begin{bmatrix} 0 & \xi_{x1} & \xi_{x2} & \xi_{x3} & 0 & 0 \\ \xi_{x1} & \rho_m(U_1+\xi_{x1}u_1) & \rho_m\xi_{x2}u_1 & \rho_m\xi_{x3}u_1 & u_1U_1\Delta\rho_l & u_1U_1\Delta\rho_g \\ \xi_{x2} & \rho_m\xi_{x1}u_2 & \rho_m(U_1+\xi_{x2}u_2) & \rho_m\xi_{x3}u_2 & u_2U_1\Delta\rho_l & u_2U_1\Delta\rho_g \\ \xi_{x3} & \rho_m\xi_{x1}u_3 & \rho_m\xi_{x2}u_3 & \rho_m(U_1+\xi_{x3}u_3) & u_3U_1\Delta\rho_l & u_3U_1\Delta\rho_g \\ 0 & \xi_{x1}\alpha_l & \xi_{x2}\alpha_l & \xi_{x3}\alpha_l & U_1 & 0 \\ 0 & \xi_{x1}\alpha_g & \xi_{x2}\alpha_g & \xi_{x3}\alpha_g & 0 & U_1 \end{bmatrix}. \tag{31}$$

Therefore, the matrix $\tilde{A}$ is given by

$$\tilde{A}=\begin{bmatrix} 0 & \xi_{x1}\beta & \xi_{x2}\beta & \xi_{x3}\beta & 0 & 0 \\ \dfrac{\xi_{x1}}{\rho_m} & \xi_{x1}u_1+U_1 & \xi_{x2}u_1 & \xi_{x3}u_1 & 0 & 0 \\ \dfrac{\xi_{x2}}{\rho_m} & \xi_{x1}u_2 & \xi_{x2}u_2+U_1 & \xi_{x3}u_2 & 0 & 0 \\ \dfrac{\xi_{x3}}{\rho_m} & \xi_{x1}u_3 & \xi_{x2}u_3 & \xi_{x3}u_3+U_1 & 0 & 0 \\ 0 & 0 & 0 & 0 & U_1 & 0 \\ 0 & 0 & 0 & 0 & 0 & U_1 \end{bmatrix}. \tag{32}$$

The eigenvalues of the preconditioned multi-phase system $\tilde{A}$ are given by

$$\lambda_1,\lambda_2,\lambda_5,\lambda_6=U_1,\qquad \lambda_3=U_1+C,\qquad \lambda_4=U_1-C, \tag{33}$$

where

$$C=\sqrt{U_1^2+\beta(\xi_{x1}^2+\xi_{x2}^2+\xi_{x3}^2)/\rho_m}. \tag{34}$$

The right eigenvector matrix is given by

$$X_i=\begin{bmatrix} 0 & 0 & \beta C & -\beta C & 0 & 0 \\ -\xi_{x2} & -\xi_{x1}\xi_{x3} & u_1\lambda_5+\dfrac{\beta\xi_{x1}}{\rho_m} & u_1\lambda_6+\dfrac{\beta\xi_{x1}}{\rho_m} & 0 & 0 \\ \xi_{x1} & -\xi_{x2}\xi_{x3} & u_2\lambda_5+\dfrac{\beta\xi_{x2}}{\rho_m} & u_2\lambda_6+\dfrac{\beta\xi_{x2}}{\rho_m} & 0 & 0 \\ 0 & \xi_{x1}^2+\xi_{x2}^2 & u_3\lambda_5+\dfrac{\beta\xi_{x3}}{\rho_m} & u_3\lambda_6+\dfrac{\beta\xi_{x3}}{\rho_m} & 0 & 0 \\ 0 & 0 & 0 & 0 & 1 & 0 \\ 0 & 0 & 0 & 0 & 0 & 1 \end{bmatrix}. \tag{35}$$

5.2. Time discretization

In the time accurate formulation, the physical-time terms in the momentum and volume fraction equations are discretized using a second-order, three-point, backward difference formula; that is

$$\Gamma_e\frac{\partial\widehat{Q}}{\partial t}=\Gamma_e\frac{1.5\widehat{Q}^{n+1,k+1}-2\widehat{Q}^{n}+0.5\widehat{Q}^{n-1}}{\Delta t}, \tag{36}$$

where n is the index of the physical-time level and k is the index of the artificial-time level. The artificial-time terms are replaced by the following implicit Euler finite-difference formula:

$$\Gamma\frac{\partial\widehat{Q}}{\partial\tau}=\Gamma\frac{\widehat{Q}^{n+1,k+1}-\widehat{Q}^{n+1,k}}{\Delta\tau}. \tag{37}$$

The governing equations (7) can be written in the following difference form:

$$\left(\Gamma_e\frac{1.5}{J\Delta t}+\Gamma\frac{1}{J\Delta\tau}+\frac{\partial A}{\partial\xi}+\frac{\partial B}{\partial\eta}+\frac{\partial C}{\partial\zeta}-\frac{\partial A^v}{\partial\xi}-\frac{\partial B^v}{\partial\eta}-\frac{\partial C^v}{\partial\zeta}-\frac{\partial\widehat{S}}{\partial\widehat{Q}}\right)\Delta Q=-\left(\frac{\partial F}{\partial\xi}+\frac{\partial G}{\partial\eta}+\frac{\partial H}{\partial\zeta}\right)^{n+1,k}$$
$$+\Gamma_e\frac{1.5\widehat{Q}^{n+1,k}-2\widehat{Q}^{n,k}+0.5\widehat{Q}^{n-1,k}}{\Delta t}+\left(\frac{\partial F^v}{\partial\xi}+\frac{\partial G^v}{\partial\eta}+\frac{\partial H^v}{\partial\zeta}+\widehat{S}\right)^{n+1,k}. \tag{38}$$

5.3. Spatial discretization

The explicit part of the viscous flux in Eq. (38) is discretized using a second-order central difference formula. The implicit part is discretized using a first-order upwind difference scheme as follows:

$$\frac{\partial A}{\partial\xi}=\frac{1}{2}\left(A-A^{+}+A^{-}\right), \tag{39}$$

where A^{+} and A^{-} are computed based on the eigenvalues of the matrix $\tilde{A}$, as follows:

$$A^{+}=\Gamma^{-1}\cdot X|\Lambda|X^{-1}, \tag{40}$$

$$\Lambda=\mathrm{diag}[\lambda_1,\lambda_2,\lambda_3,\lambda_4,\lambda_5,\lambda_6], \tag{41}$$

$$A^{-}=A-A^{+}. \tag{42}$$

The explicit part of the convective flux vector is discretized using a third- or first-order Roe scheme, depending on the gradients of the flow variables in the flow field. The flux difference splitting scheme is constructed based on the eigenvalues and eigenvectors of the Jacobian matrix $\tilde{A}$.

Considering the derivative of the convective flux in the ξ-direction, we use the following difference formula for the flux derivatives:

$$\frac{\partial F}{\partial\xi}=\frac{F_{i+1/2}-F_{i-1/2}}{\Delta\xi}. \tag{43}$$

The convective flux at the mid-cell points is computed using the following equation:

$$F_{i+1/2}=\frac{1}{2}\left[F(Q_{i+1})+F(Q_i)-\phi_{i+1/2}\right], \tag{44}$$

where $\phi_{i+1/2}$ is the dissipation term.

For a first-order upwind difference scheme, the dissipative term is given by

$$\phi_1=\Delta F^{+}_{i+1/2}-\Delta F^{-}_{i+1/2}. \tag{45}$$

For a third-order upwind difference scheme,

$$\phi_3=-\frac{1}{3}\left(\Delta F^{+}_{i-1/2}-\Delta F^{+}_{i+1/2}+\Delta F^{-}_{i+1/2}-\Delta F^{-}_{i+3/2}\right), \tag{46}$$

where

$$\Delta F^{\pm}_{i+1/2}=\Gamma\cdot\tilde{A}^{\pm}(\overline{Q})\cdot\Delta Q, \tag{47}$$

$$\overline{Q}=\frac{1}{2}(Q_{i+1}+Q_i), \tag{48}$$

$$\Delta Q=Q_{i+1}-Q_i. \tag{49}$$

Flux limits are usually used to avoid spurious numerical oscillations [20]. In the current work, an indicator function is defined depending on the gradients of the flow variables, to determine the accuracy of the flux difference scheme. The indicator function is defined in terms of the following vector:

$$\eta_1 = \frac{4(Q_{i+1} - 2Q_i + Q_{i-1})}{|(Q_{i+1} + 2Q_i + Q_{i-1})|}, \tag{50}$$

$$\eta = \min\bigl(\max(\eta_1), 1\bigr). \tag{51}$$

Thus, the dissipation part in the flux difference scheme is defined as follows:

$$\phi_{i+1/2} = (1 - \eta)\phi_3 + \eta\phi_1.$$

6. Boundary conditions

Different boundary conditions are used in the simulations, including inflow, outflow, no-slip, and symmetric boundary conditions. All of the boundary conditions are treated implicitly in the code to reduce the restriction on the time step and to increase the stability of the code. For the inflow boundary, the velocity components and the volume fractions are specified, while the pressure is extrapolated from the interior points. At the outflow boundary, the pressure is specified, whereas the velocity components and the volume fractions are extrapolated from the computational domain. At the walls, the velocities are set equal to zero, whereas the volume fraction and the pressure are extrapolated. At the line of symmetry (centerline), the normal velocity to the centerline is set equal to zero while the derivatives normal to the line of symmetry for the tangential velocities, the volume fraction, and the pressure are set equal to zero. In addition, similar boundary conditions are needed for the turbulent quantities.

7. Results

The cavitating flows are computed over different semi-infinite projectile geometries, such as hemispherical, ogive, conical, and blunt bodies. In addition, the effect of the angle-of-attack on the bubble shape and the surface-pressure distribution is investigated. The computations are done for different cavitation numbers and a Reynolds number of 10^5. The vapor–water density ratio is assumed to be 0.0001 in all the simulations. C-grid of dimensions $80 \times 32 \times 124$ in the normal, azimuthal, and spanwise directions, respectively, is used. The computations have been also performed on coarser grids and that, since the results on two subsequent grids are practically coincident, only the results on the finer grid are reported. The grid is clustered in the normal direction near the body surface and in the spanwise direction as shown in Fig. 1(a). A minimum grid size of 0.001 is used in the normal direction on the body surface. The computational domain is composed of two blocks. The first block is generated only for the nose part to ensure that the grid lines are normal to the boundaries while the second block is constructed for the cylindrical part.

Two-time levels are used for the unsteady computations. The artificial-time step is restricted by the CFL condition, which allows for a larger time step due to the implicit treatment of the governing equations and the boundary conditions. A small value of the physical time step is used in the simulations in order to resolve accurately the transients of the cavitating flow, which occur very rapidly. An optimum convergence rate is obtained for a compressibility parameter β of 5.

The current numerical method can be used to compute single-phase as well as multi-phase flows on cavitating bodies. A single-phase flow on a hemispherical body is first considered to validate the method, as in Fig. 1(b). A steady state is

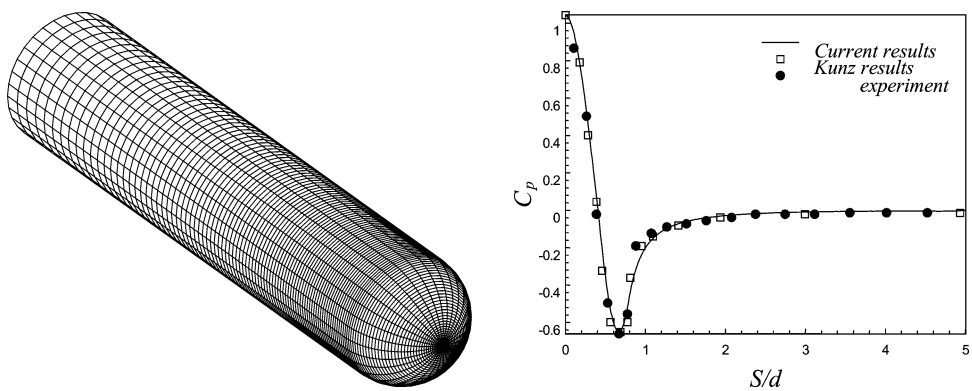

(a) (b)

Fig. 1. Single-phase flow on the surface of a hemispherical body. (a) Computational grid (dimensions $80 \times 32 \times 124$). (b) Pressure-coefficient distribution.

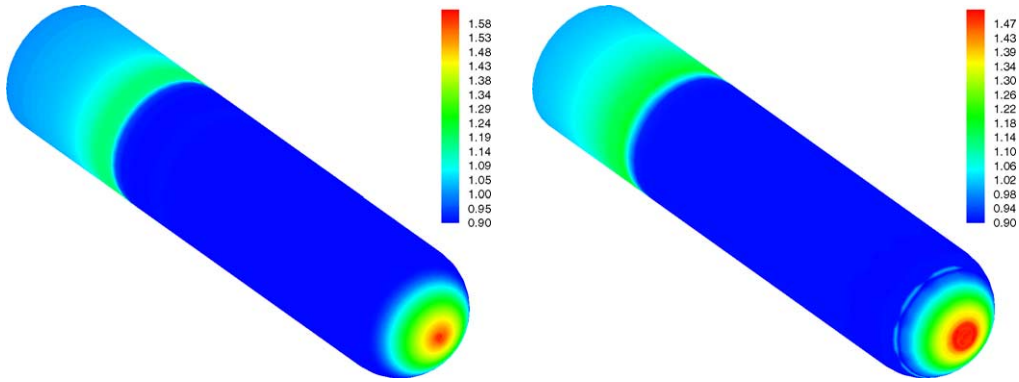

(a) (b)

Fig. 2. Surface-pressure contours for the cavitating flow over a hemispherical body ($\sigma = 0.2$): (a) without gas injection and (b) with gas injection.

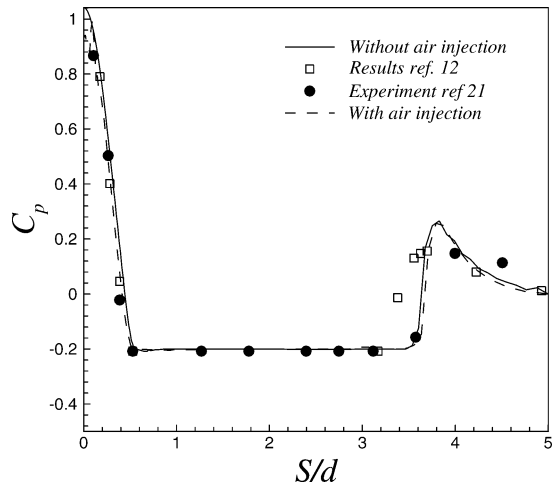

Fig. 3. Pressure-coefficient distribution over a hemispherical body for a cavitating flow with and without gas injection, $\sigma = 0.2$.

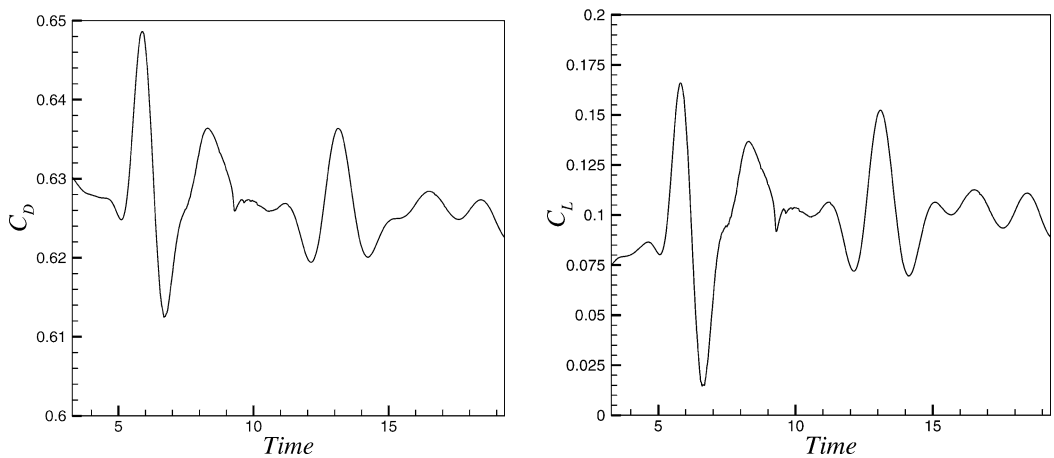

(a) (b)

Fig. 4. Time variation of the drag and lift coefficients for the cavitating flow over the hemispherical body ($\sigma = 0.35$) with an angle of attack ($\alpha. = 10°$). (a) Drag coefficient. (b) Lift coefficient.

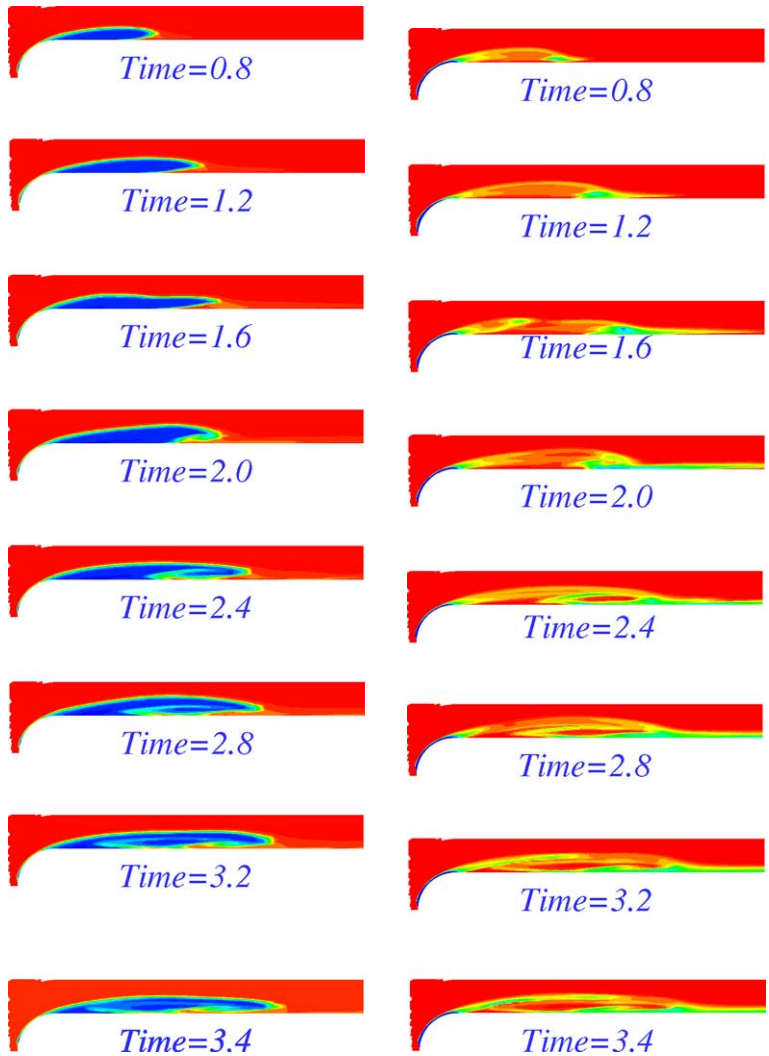

Fig. 5. Water and gas volume fractions for the cavitating flow over the hemispherical body ($\sigma = 0.2$) with gas injection on the body nose. (a) Liquid volume fraction. (b) Gas volume fraction.

obtained for this single-phase flow at the given conditions. The variation of the pressure coefficient along the body surface is compared with the experimental data of Rouse and McNown [21] and computational results of Kunz et al. [12]. The results are in good agreement with both the experimental and computational results. The single-phase computations indicate the maximum cavitation number at which the water might evaporate for specified Reynolds number. This cavitation number corresponds to the minimum pressure coefficient on the body surface.

Three different cavitating flows over the hemispherical body are computed at a cavitation number of 0.2. In the first case, natural cavitation on the body is computed. In the second case, the effect of ventilated cavitation on the flow is considered by injecting a non-condensable gas near the nose over a small length of the body surface. The gas is injected normal to the projectile surface and the injection is assumed to be at a distance of 0.2 the projectile diameter from the nose measured along the axis. The maximum velocity of the injected gas is assumed to be twice the freestream velocity, and a parabolic velocity profile in the spanwise direction is used for the injection. In the third case, natural cavitation is computed at an angle of attack. The surface pressure contours are presented in Fig. 2 (a) and (b) for the natural and ventilated cavitation flows. For both flows, the pressure increases at the end of the vapor bubble on the surface although the bubble end is covered by a mixture of non-condensable gas and water for the ventilated case. The pressure jump at the bubble closure is attributed to the water jet reentry in both the ventilated and natural cavitation. Therefore, similar pressure jumps are obtained because water content in the mixture reentering

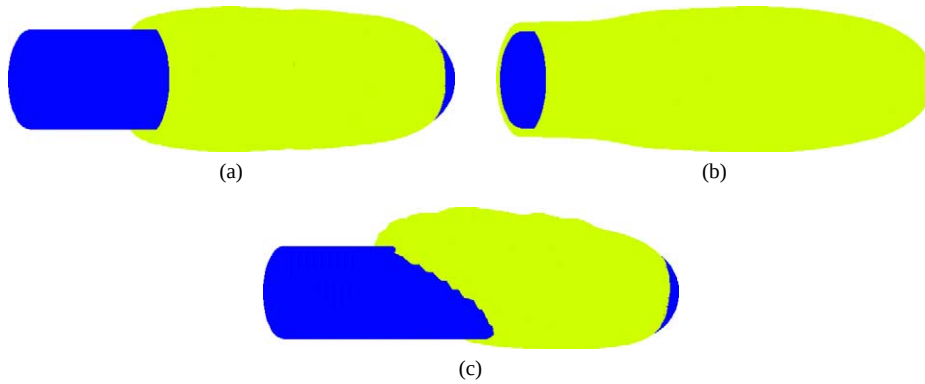

Fig. 6. Bubble shapes for the cavitating flow over a hemispherical body ($\sigma = 0.2$). (a) Without gas injection and zero angle of attack, (b) with gas injection and zero angle of attack, (c) without gas injection and five degrees angle of attack.

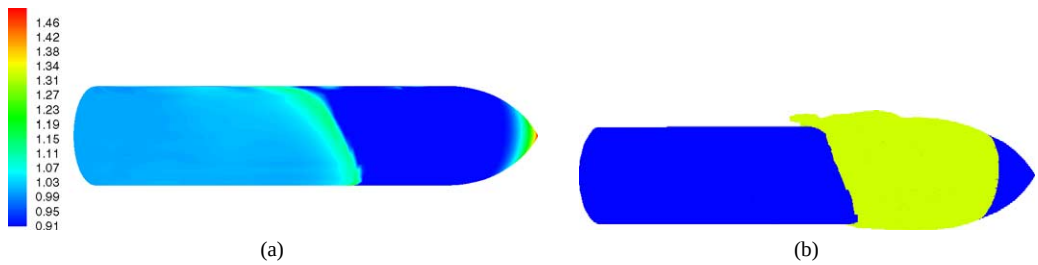

Fig. 7. The cavitating flow over a 1-cliber ogive body at 2.5° angle of attack ($\sigma = 0.2$): (a) surface pressure distribution, (b) bubble shape.

the bubble is high. For the natural and ventilated cavitations, the results are compared with available experimental and other computations in Fig. 3. The results indicate that the ventilated cavitation has a small effect on the surface pressure. On the other hand, the viscous drag on the body is reduces significantly due to the gas injection.

The time variation of the hydrodynamic loads on the cavitating hemispherical body for 10 degrees angle of attack is introduced in Fig. 4 (a) and (b). The cavitation number is assumed to be 0.35 for this case. The results indicate that both the lift and drag are oscillating at the same frequencies. The lift and drag forces have a steady state component. The amplitude of the lift oscillations is greater than the drag oscillations.

The time sequence of the bubble shape over a cavitating hemispherical body with gas injection is presented in Fig. 5 (a) and (b). As the pressure in the flowfield becomes lower than the vapor pressure, a bubble grows on the projectile surface. Due to the bubble closure on the surface, the pressure increases near the bubble end causing the bubble to collapse. In addition, a mixture of non-condensable gas and water is pushed into the bubble due to the large pressure difference near the bubble end and a jet penetrates deep into the bubble. This jet reentrance causes the bubble to break off at certain point. As a result, the pressure jump at the bubble end disappears, causing the jet to slow down until the cycle is repeated. The contours of the gas volume fraction are shown in Fig. 5(b). The gas covers the vapor bubble and the whole surface of the body. In addition, a jet of gas-water mixture moves under the vapor bubble. As a result of the gas flow under the vapor bubble and on the body surface, the viscous drag is significantly reduced. The bubble shapes of the cavitating flows over a hemispherical body are shown in Fig. 6. Most of the body is covered by a vapor–gas bubble for the ventilated cavitation. For the natural cavitation, the vapor bubble covers part of the body at a cavitation number of 0.2. At 5 degrees angle of attack, the bubble shape becomes unsymmetric in the angular direction causing a pressure variation in this direction.

In Fig. 7(a), the surface pressure contours and the bubble shape are presented for the cavitating flow over 1-caliber ogive body with a small angle of attack. Unsymmetrical bubble shape associated with a pressure variation in the angular direction is obtained for this case. The flow can be clearly seen to be highly three-dimensional. As a result of this 3-D flow, redistribution of forces and moments occurs on the body surface. We noticed that the ogive body produces a drag force less than that produced by the hemispherical and conical bodies at the same condition. This reduction in the drag force is caused by the reduction of the drag on the nose since the pressure distribution near the nose varies with the nose geometry.

Single- and two-phase flows over an axisymmetric blunt body are computed at different cavitation numbers. The computation of this case is very sensitive to the refinement of the grid at the sharp corner of the body where large flow gradients might exist. Very fine grids produce high numerical oscillations near the corner where the turbulence models might not produce enough

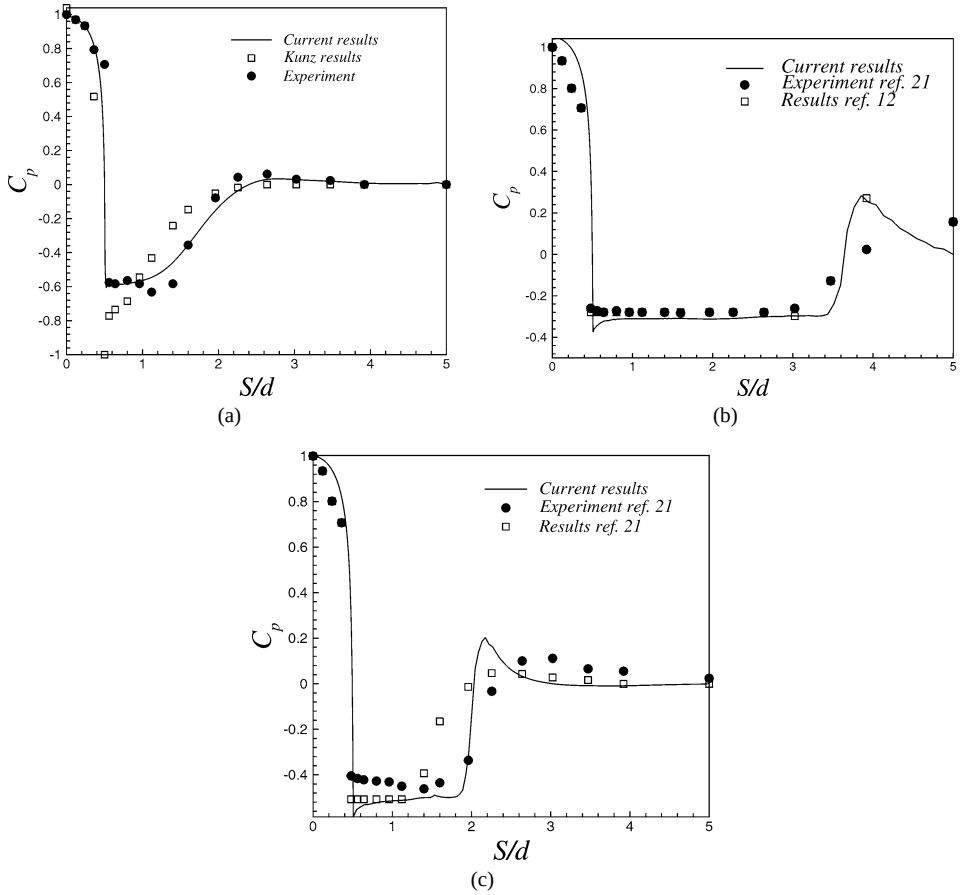

Fig. 8. Pressure-coefficient distribution over the surface of an axisymmetric blunt body. (a) Single-phase flow. (b) Cavitating flow ($\sigma = 0.5$). (c) Cavitating flow ($\sigma = 0.3$).

Fig. 9. Bubble shape of the cavitating flow over an axisymmetric blunt body: (a) $\sigma = 0.5$, (b) $\sigma = 0.3$.

dissipation to smooth out the solution. Therefore, the computational grid for this case should be chosen carefully in order to resolve this flow accurately. The single-phase flow computations agree with the experiment as shown in Fig. 8(a). Moreover, the cavitating flow over the blunt body is computed at two different cavitation numbers. In both cases, the results agree with the experiment as shown in Fig. 8 (b) and (c). For the computations, the pressure jump at the end of the bubble is sharper than the experiment. This result could be referred to the inability of the turbulence model to produce enough dissipation for this case. The bubble shapes are presented in Fig. 9 (a) and (b) at cavitation numbers of 0.3 and 0.5. The effect of the cavitation number

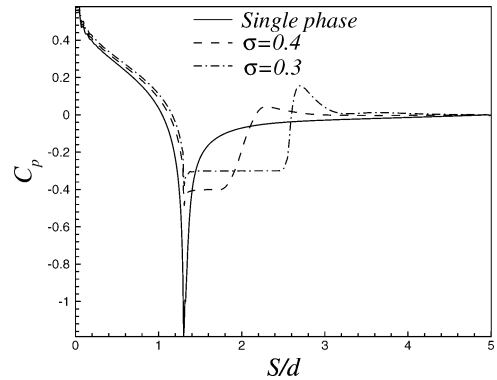

Fig. 10. Pressure-coefficient distribution over the surface of an axisymmetric conical body.

on the bubble size can be seen from the figure. At the specified cavitation numbers, a water jet reentry is noticed at the end of the bubble.

In Fig. 10, the pressure coefficient distribution over the surface of a conical body is presented for single-phase and cavitating flows. The cone half-angle is 22.5° for this case. The single-phase flow computations indicate that the flow cavitates at a maximum cavitation number of 1.2. For the cavitating flows, a pressure jump can be seen at the bubble closure. The results indicate that the bubble size for this geometry is smaller than the bubble size for the hemispherical and blunt bodies.

8. Conclusions

A numerical method is developed to solve the unsteady incompressible Navier–Stokes equations for multi-phase flows. A new preconditioning matrix is introduced by adding new artificial terms to the governing equations and hence a new eigensystem is derived for the Jacobian matrices. The convective flux vector is discretized using an upwind flux difference splitting scheme on a structured grid. The equations are integrated implicitly in time and the resulting linear system is solved iteratively using the Gauss–Seidel line-relaxation method. All of the boundary conditions are treated implicitly in the code to reduce the restriction on the time step. A zonal turbulence model is employed for the computation of the eddy viscosity and the model is solved separately from the governing equations to alleviate the system stiffness and to reduce the computational time. Cavitating flows over different geometries are computed for different cavitation numbers with and without gas injection. The computations indicate that the viscous drag is significantly reduced due to gas injection on the body nose. Moreover, the one-caliber ogive body produced less drag than the hemispherical and conical bodies due to the reduction of the induced drag on the body nose. In general, the results are in good agreement with both the experimental results and other published computations.

Acknowledgements

This work was supported by the Office of Naval Research under the Multidisciplinary University Research Initiative (MURI) on Nonlinear Active Control of Dynamical Systems, Contract Number N00014-96-1-1123.

References

[1] F.H. Harlow, J.E. Welch, Numerical calculation of time-dependent viscous incompressible flow of fluid with free surface, Phys. Fluids 8 (12) (1965) 2182–2189.
[2] B.J. Daly, Numerical study of density-current surges, Phys. Fluids 11 (1968) 15–30.
[3] C.S. Peskin, Numerical analysis of blood flow in the heart, J. Comput. Phys. 25 (1977) 220–229.
[4] S.O. Unverdi, G.A. Tryggvason, Front-tracking method for viscous, incompressible multi-fluid flows, J. Comput. Phys. 100 (1992) 25–37.
[5] S.O. Unverdi, G.A. Tryggvason, Computations of multi-fluid flow, Physica D 60 (1992) 70–83.
[6] A. Kubota, H. Kato, H. Yamagauchi, Cavity flow predictions based on the Euler equations, J. Fluid Mech. 240 (1992) 59–96.
[7] H. Lemonnier, A. Rowe, Another approach in modeling cavitating flows, J. Fluid Mech. 195 (1988) 557–570.
[8] Y. Delannoy, J.L. Kueny, Cavity flow predictions based on the Euler equations, ASME Cavitation and Multi-Phase Flow Forum 109 (1990) 153–158.

[9] M.E. Jannens, S.J. Hulshoff, H.W.M. Hoijmarks, Calculation of unsteady attached cavitation, AIAA Paper 97-1936, 1997.
[10] C.L. Merkle, J. Feng, P.E.O. Buelow, Computational modeling of the dynamics of sheet cavitation, in: Proceedings of the 3rd International Symposium on Cavitation, Grenoble, France, 1998.
[11] R.F. Kunz, D.A. Boger, H.J. Gibeling, T.R. Govindan, A preconditioning Navier–Stokes method for two-phase flows, in: Proceedings of the 14th AIAA CFD conference, Norfolk, VA, AIAA Paper 99-3329, 1999.
[12] R.F. Kunz, D.A. Boger, T.S. Chyczewski, D.R. Stineberg, H.J. Gibeling, T.R. Govindan, Multi-phase CFD analysis of natural and ventilated cavitation about submerged bodies, in: Proceedings of 3rd ASME/JSME Joint Fluids Engineering Conference, ASME Paper FEDSM99-7364, 1999.
[13] V. Ahuja, R. Hosangadi, R. Ungewitter, S.M. Dash, A hybrid unstructured mesh solver for multi-fluid mixtures, in: Proceedings of the 14th AIAA CFD conference, Norfolk, VA, AIAA Paper 99-3330, 1999.
[14] I. Toumi, A. Kumbaro, H. Paillere, Approximate Riemann solvers and flux vector splitting schemes for two-phase flow, in: Proceedings of the 30th Computational Fluid Dynamics, in: von Karman Inst. Lecture Ser., vol. 3, 1999.
[15] F.R. Menter, Zonal two-equation k–ω turbulence models for aerodynamic flows, AIAA Paper 93-1906, 1993.
[16] S.E. Rogers, F. Menter, P.A. Durbin, N.N. Mansour, A comparison of turbulence models in computing multi-element airfoil flows, AIAA Paper 94-0291, 1994.
[17] D.C. Wilcox, Multiscale model for turbulent flows, AIAA J. 26 (11) (1988) 1311–1320.
[18] W.P. Jones, P.E. Launder, The calculation of low Reynolds number phenomena with a two-equation model of turbulence, Int. J. Heat Mass Transfer 16 (1973) 1119–1130.
[19] P.L. Roe, Approximate Riemann solvers, parameter vectors, and difference schemes, J. Comput. Phys. 43 (1981) 357–372.
[20] S.R. Chakravarthy, K.Y. Szema, U.C. Goldberg, J.J. Gorski, Application of a new class of high accuracy. TVD schemes to the Navier–Stokes equations, in: AIAA 23rd Aerospace Sciences Meeting, Reno, NV, AIAA Paper 85-0165, 1985.
[21] H. Rouse, J.S. McNown, Cavitation and Pressure Distribution, Head Forms at Zero Angle of Yaw, in: Stud. Engrg., vol. 32, State University of Iowa, 1948.